Directed energy deposition of Invar 36 alloy using cold wire pulsed gas tungsten arc welding

Effect of heat input on the microstructure and functional behaviour

Sood, Arjun; Schimmel, Jim; Ferreira, Vitoria M.; Bosman, Marko; Goulas, Constantinos; Popovich, Vera; Hermans, Marcel J.M.

DOI
10.1016/j.jmrt.2023.06.280

Publication date
2023

Document Version
Final published version

Published in
Journal of Materials Research and Technology

Citation (APA)
Sood, A., Schimmel, J., Ferreira, V. M., Bosman, M., Goulas, C., Popovich, V., & Hermans, M. J. M. (2023). Directed energy deposition of Invar 36 alloy using cold wire pulsed gas tungsten arc welding: Effect of heat input on the microstructure and functional behaviour. *Journal of Materials Research and Technology*, *25*, 6183-6197. https://doi.org/10.1016/j.jmrt.2023.06.280

JOURNAL OF MATERIALS RESEARCH AND TECHNOLOGY 2023;25:6183–6197

Available online at www.sciencedirect.com

jmr&t Journal of Materials Research and Technology

journal homepage: www.elsevier.com/locate/jmrt

Directed energy deposition of Invar 36 alloy using cold wire pulsed gas tungsten arc welding: Effect of heat input on the microstructure and functional behaviour

Arjun Sood [a,*], *Jim Schimmel* [a], *Vitoria M. Ferreira* [a], *Marko Bosman* [b], *Constantinos Goulas* [c], *Vera Popovich* [a], *Marcel J.M. Hermans* [a]

[a] *Department of Materials Science and Engineering, Delft University of Technology, the Netherlands*
[b] *GKN Aerospace, Fokker Aerostructures B.V., the Netherlands*
[c] *Faculty of Engineering Technology, University of Twente, the Netherlands*

ARTICLE INFO

Article history:
Received 7 April 2023
Accepted 25 June 2023
Available online 13 July 2023

Keywords:
Gas tungsten arc welding
Invar
Cracking
Heat input
Thermal expansion

ABSTRACT

Invar alloys exhibit low thermal expansion and are useful in applications requiring dimensional stability when subject to temperature changes. Conventional production of Invar faces certain challenges that can be offset by exploiting additive manufacturing processes. This study employed pulsed gas tungsten arc welding (GTAW) to deposit Invar 36 alloy blocks at five heat inputs (HI) ranging from 200 to 550 J mm^{-1}. The results show that the microstructure comprised of columnar grains and remained in the austenitic phase regardless of the HI. Ductility dip cracking was found to prevail in all the blocks except the block deposited at the lowest HI. The decreased susceptibility to cracking with a reduction in the HI was due to the preservation of the grain boundary area, consequently leading to an improved partitioning of strain among the grain boundaries. On lowering the HI from 550 to 200 J mm^{-1} the average yield strength, tensile strength and elongation improved by 16%, 23% and 38%, respectively. The HI had a negligible effect on the mean linear coefficient of thermal expansion (CTE) in different temperature ranges as the CTE values were nearly identical between the blocks deposited at 200 and 550 J mm^{-1}. In general, the CTE in the building direction was slightly higher than the travel direction, with a maximum difference between the CTE of the two directions being 15%. In summary, this work demonstrates the application of the cold wire GTAW process as an alternative to conventional/laser based methods for realizing the functional properties of Invar.

1. Introduction

The binary Fe–Ni system presents a class of functional alloys that have uniquely low thermal expansion. They are referred to as the Invar alloys, where the term Invar stands for invariance to temperature [1]. The dimensional stability in Invar alloys is observed below the Curie temperature and is a result of a temperature dependent interaction between the lattice expansion/contraction and spontaneous volume

---

* Corresponding author.
E-mail address: a.sood@tudelft.nl (A. Sood).

https://doi.org/10.1016/j.jmrt.2023.06.280

magnetostriction [2,3]. The minimum linear thermal expansion coefficient (CTE) in the binary Fe–Ni system is observed at a Ni content of about 36 wt % (Invar 36 alloy) [4]. For comparison, the mean CTE of Invar 36 and SS316L between 293 K and 373 K are 1.6 μm m^{-1} K^{-1} and 16 μm m^{-1} K^{-1}, respectively [5,6]. As such, Invar alloys are used in precision instruments, aerospace moulding tools and storage tanks/pipelines for use at cryogenic temperatures [4,7–9]. Invar products in the aerospace sector are traditionally fabricated using subtractive processes, like milling and turning [10]. However, machining of Invar can be challenging due to certain physical aspects of this alloy such as, high rates of work hardening and low thermal conductivity [11]. Additionally, subtractive techniques often result in the generation of significant material waste [12,13]. In this regard, additive manufacturing (AM) techniques are a good alternative as they are not associated with such drawbacks [14]. The most common metal AM techniques are based on either using a laser, electric arc, or electron beam as the heat source [15,16]. The raw material/consumable that is used in these processes is available in the form of metal powders or wires. The combination of using an electric arc with metal wires, known as wire and arc additive manufacturing (WAAM), is one of the directed energy deposition (DED) techniques that may be well suited for fabricating Invar products especially in the aerospace sector [10,17]. This is attributed to the lower cost of the metal wires and high deposition rates achieved in WAAM in comparison to metal powder-based AM [13,18].

Recently, multiple studies have emerged that address the microstructure/properties of Invar based on laser-powder processing [11,19–25]. In contrast to this, the body of literature pertaining to WAAM of Invar is limited. Veiga et al. used gas metal arc welding (GMAW) and plasma arc welding (PAW) to deposit two thin wall structures of Invar 36 for a comparative study [26]. The mechanical properties were quantified, and the results indicate directional anisotropy in the elongation of the samples deposited with the PAW process. Aldalur et al. in continuation of the above work reported the thermal properties of the as-deposited Invar 36 by GMAW and PAW processes in another study [27]. The results showed higher mean CTEs of Invar deposited with the PAW process, whereas the CTE of the Invar deposited with the GMAW process were comparable to conventionally processed Invar. Fowler et al. used metal inert gas (MIG) welding to fabricate different geometries (walls, tubes, and overhangs) with a commercially available Invar 36 alloy (CF36 filler wire) [28]. The thermal expansion of the deposited Invar was found to be satisfactory for their purpose. This study was limited to the assessment of the printability of Invar and excluding the microstructure related aspects of the deposits. The literature pertaining to the welding of Invar, especially multi-pass welds, can help predict the behaviour of Invar in a process like WAAM, since it is essentially based on the principles of welding. Among these studies a common observation is the presence of intergranular cracks [8,29–31]. Naturally, such defects are undesirable and may lead to premature failure during the service life of a product in load bearing applications. Therefore, to further establish the application of WAAM to Invar there is an explicit need to develop an understanding of the resulting microstructure and properties. To build on this we have performed a systematic experimental study followed by extensive characterisation to understand the response of the Invar alloy to DED-WAAM. Gas tungsten arc welding (GTAW) was utilised in this study to deposit blocks using a commercially available Invar 36 wire at five heat inputs ranging from 200 J mm^{-1} to 550 J mm^{-1}. The effect of the heat input on the microstructure, defects and the microhardness of the deposited blocks was investigated. The chemical analysis on the deposited blocks was performed using X-ray fluorescence (XRF). A further evaluation of the microstructure was realised using electron backscatter diffraction (EBSD), along with phase identification using X-ray diffraction (XRD) on the blocks deposited at the extremes of the heat input, i.e., 200 and 550 J mm^{-1}. Lastly, two larger blocks were deposited using the parameters corresponding to the extremes of the heat input to quantify the mechanical properties and the linear CTE of the deposited Invar alloy.

2. Research methodology

2.1. *Experimental overview*

A Migatronic TIG COMMANDER 400 AC/DC was used as the power source for depositing 80 × 15 × 15 mm^3 blocks of Invar. All the experiments were performed in the pulsed current mode using argon as a shielding gas at a flow rate of 10 L min^{-1}. The consumable was a 1.2 mm diameter wire sourced from Voestalpine Böhler Welding, commercially known as 3Dprint AM Mold 36 (alloy Fe–Ni36). The chemical composition of the wire and the deposition parameters corresponding to the five blocks (A to E) are listed in Tables 1 and 2, respectively. The deposition was carried out unidirectionally (along X direction) and the wire was front fed towards the leading edge of the weld pool as shown schematically in Fig. 1. The current and the voltage profiles during the deposition process were measured using a Triton data logger. This data was used for calculating the instantaneous power (*IP*) based on equation (1) and in conjunction with equation (2) for determining the heat input (*HI*) by assuming a process efficiency (η) of 0.7 [32,33]. Where, I_i is the instantaneous current [A], U_i is the instantaneous voltage [V], and *TS* is the travel speed [mm s^{-1}]. The calculated heat input was rounded off to the nearest ten as listed in Table 2.

Table 1 – Chemical composition of the Invar wire as specified by the supplier (*element content less than the specified number).

Elements, wt. %	C	Si*	Mn	Cr*	Mo*	Co*	P*	S*	Ni	Fe
Alloy Fe–Ni36	0.05	0.10	0.20	0.50	0.50	1.00	0.01	0.01	34–38	Bal.

Table 2 – The process parameters used in this study for the deposition of the blocks (A to E). TS- travel speed, WFS- wire feed speed, I_{Base}-base current, I_{peak}-peak current, t_{base}-base time, t_{peak}-peak time, U_{Ave}-average voltage and HI- heat input.

Parameters	TS mm s^{-1}	WFS mm s^{-1}	I_{Base} A	I_{Peak} A	t_{Base} s	t_{Peak} s	U_{Ave} V	HI J mm^{-1}
A	4.6	22.0	81	180	0.2	0.20	10.0	200
B	4.5	28.0	110	220	0.2	0.15	10.3	250
C	3.8	30.0	120	240	0.2	0.20	10.6	350
D	3.5	39.0	133	265	0.2	0.20	11.4	450
E	3.3	50.0	135	300	0.2	0.20	12.0	550

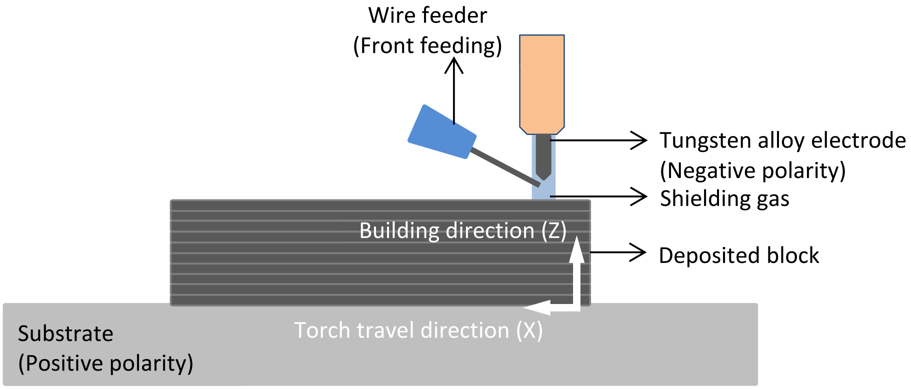

Fig. 1 – Schematic of the GTAW deposition process used in this study.

$$IP = \frac{1}{n}\sum_{n=1}^{n}(I_i \bullet U_i) \qquad \text{Equation 1}$$

$$HI = \frac{IP \bullet \eta}{TS} \qquad \text{Equation 2}$$

The dimensions of the single beads that were used to create the blocks were also measured. Optical microscopy was utilised for this purpose and the measured characteristics are schematically shown in Fig. 2, where θ is the wetting angle, w is the width, H is the height, P is the penetration, A and B are the cross-sectional areas. The tip angle of the tungsten electrode was 40° and 30° while deposing blocks B to E and block A, respectively. The substrate for the experiments were a low carbon structural steel plates of 25 mm thickness. The first two layers of the blocks were not considered for any analysis due to the dilution with base plate. This was based on preliminary energy dispersive spectroscopy (EDS) measurements performed on the builds and indicated that the Invar composition of 36 wt% Ni was attained after the second layer. The substrate plates were ground to remove any oxides and cleaned with isopropanol prior to the experiments. The maximum inter-pass temperature was limited to 423 K during the deposition and was checked using a K-type thermocouple [34].

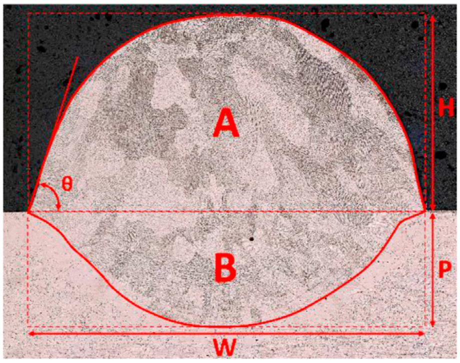

Fig. 2 – Schematic of the weld bead dimensions analysed from the bead-on-plate experiments.

2.2. *Microstructural characterisation*

Four transverse sections were taken from each block at similar locations for observing the microstructure. The samples were first subjected to mechanical grinding using SiC papers (P180 to P4000). Following grinding, samples were polished using a 3 and a 1 μm diamond suspension for 6 and 10 min, respectively. Chemical etching was performed on polished samples using the Kalling's 2 reagent for 5–10 s to reveal the microstructure. The microstructural features were observed using a Keyence VHX-5000 optical microscope and a JEOL JSM-6500F™ scanning electron microscope (SEM). Micro hardness (Vickers hardness) measurements were performed on etched samples at room temperature using a Struers DuraScan hardness tester following the ISO 6507-1 standard [35]. The chemical composition of the deposited blocks was quantified using X-ray fluorescence (XRF) with a Panalytical Axios^{mAX} WD-XRF spectrometer. Phase analysis was also performed using X-ray diffraction with a Bruker D8 Advance diffractometer.

Additionally, samples were taken from the blocks deposited at the extremes of the heat input for electron backscatter diffraction (EBSD) analysis. These samples were polished using colloidal silica for 40 min in addition to the earlier stated

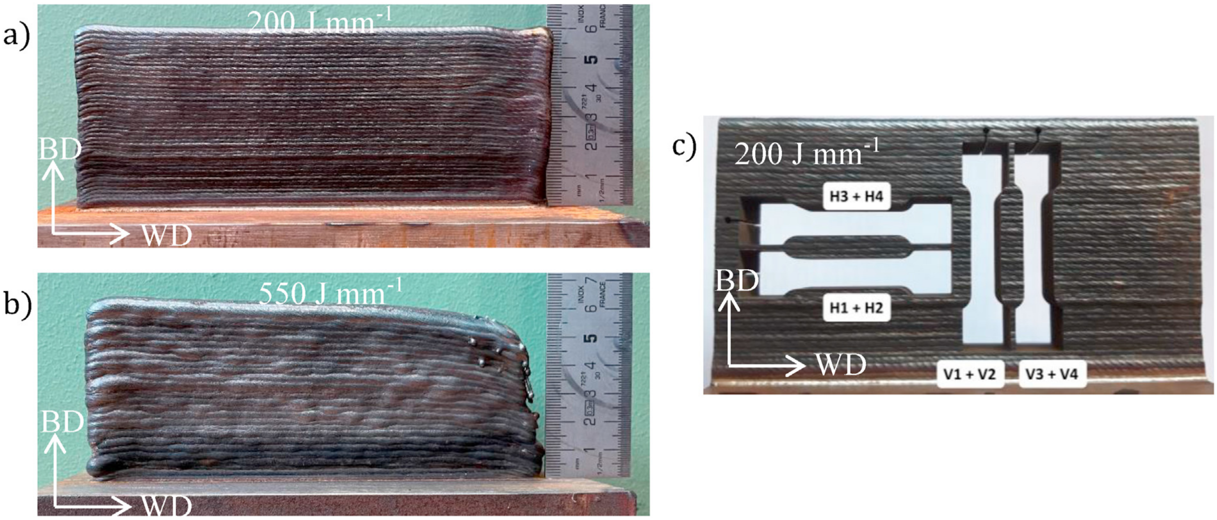

Fig. 3 – The as-deposited blocks A1 and E1 at the extreme conditions of the heat input for extracting tensile specimens in (a) and (b), respectively. V (1–4) and H (1–4) indicates the marking of the vertical (Z) and horizontal (X) samples, respectively in (c). BD-building direction (Z) and WD-welding/travel direction (X).

polishing procedure. A Thermo Scientific™ Helios™ G4 PFIB UXe SEM equipped with a EDAX detector was used for the EBSD analysis, and the results were processed using the TSL OIM software. A step size of 0.5 μm was used to map areas of 1×1 mm^2 in all the scans. The current and the acceleration voltage were 3.2 nA and 20 kV, respectively.

2.3. *Tensile testing*

The extreme conditions of the heat input, i.e., 200 and 550 J mm^{-1} were used for depositing two larger blocks of $150 \times 20 \times 60$ mm^3 as shown in Fig. 3 (a) and (b). The blocks will be referred to as A1 and E1 from here on, and were used for extracting tensile specimens. The sample geometry and testing procedure was based on the guidelines outlined in the ISO 6892-1 standard [36]. The samples were extracted with their main axis oriented parallel to the building (Z) and the welding/travel direction (X) to quantify the properties in two directions as shown in Fig. 3 (c), for the low heat input block (A1). The sample extraction procedure was similar for the high heat input block (E1). A total of eight samples were tested per block, comprising of four samples from the two directions (X and Z). The tensile tests were performed at room temperature using an INSTRON® 5500R machine using a strain rate of 1 mm min^{-1}. Following the tests, the fracture surface of the specimens was analysed using a SEM in the secondary electron mode at an acceleration voltage of 15 kV.

2.4. *Dilatometry*

A Linseis TMA PT1000 thermo-mechanical analyser was used for evaluating the linear CTE of the as-deposited Invar. Dilatometry was performed on samples taken from the blocks deposited at the extremes of the heat inputs (200 and 550 J mm^{-1}). Cylindrical specimens of 4 mm diameter and 10 mm length were extracted using wire electronic discharge machining. Two samples were extracted from each block (A1 and E1) comprising of one sample per direction (X and Z). The testing was performed in accordance with the ASTME 831-14 standard in a temperature range between room temperature and 673 K with a heating rate of 5 K min$^{-1.}$ [37].

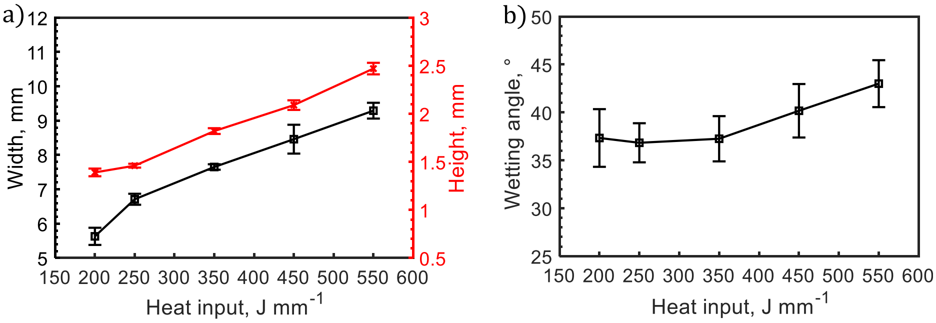

Fig. 4 – Dimensions and wetting angle of the weld beads corresponding to the five heat inputs used for the deposition of the blocks in (a) and (b), respectively.

3. Results and discussion

3.1. *Macro and microstructural characterisation*

Bead-on-plate experiments were initially performed to optimise the deposition parameters for the Invar wire used in this study. The criteria for selecting the deposition parameters stated in Table 2 was based on the wetting angle of the resulting weld beads. The weld beads with a wetting angle in the range of 35°–45° were chosen for deposition with the aim to avoid lack of fusion defects during overlapping of the weld beads. The dimensional characteristics of the weld beads corresponding to the five heat inputs used in this study are shown in Fig. 4 (a) and (b). In general, it is observed that the size and the wetting angle of the weld beads increases with the heat input. This is due to an increase in the deposition rate with the increasing heat input. The process parameters corresponding to these weld beads were considered stable for deposition of the blocks due to the dimensional stability of the weld beads. This is reflected in the relatively low scatter observed in the dimensional characteristics of the weld beads. The macroscopic overview of the blocks corresponding to the five heat inputs is shown in Fig. 5. The blocks did not show the presence of lack of fusion related defects (in four transverse sections), essentially due to limiting the wetting angle of the weld beads to 45°. Since these blocks were deposited unidirectionally, the ends of the blocks tended to taper off. This was due to the start/stop of the arc and had the largest effect on block E. In contrast, the low heat input used for the deposition of block A, resulted in a good geometrical stability of the block. An example of the tapering in the high heat input (550 J mm^{-1}) condition is visible in Fig. 3 (b). In general, the macroscopic deposition quality of the blocks improved with decreasing the heat input. The microstructure of the blocks was found to be dominated by columnar grains as shown in Figs. 5 and 6. The columnar grains grow epitaxially in the blocks and tend to be oriented parallel to the building direction since grain formation is favoured along the direction of maximum heat flow [38]. The substructure mainly comprises of cellular features as pointed out in Fig. 6, with an occasional presence of columnar dendrites. The different substructures arise from local variations in the solidifying conditions in the melt pool from the combined effect of the temperature gradient and the solid-liquid interface growth velocity. The existence of such microstructural features is typically observed in single phase austenitic alloys. In general the columnar grains were found to extend through multiple layers in all the blocks. Moreover, in the case of block E extensive grain coarsening is observed in the top half of the block. This is indirectly reflected in the micro hardness measurements as shown in Fig. 7. Also, the differences in the morphology of the grains observed in blocks A and E are evident when comparing Fig. 5 (A) and (E). The tendency of grain coarsening, as deposition proceeds, increases with the heat input as block E shows the maximum difference between the hardness measured at 5 mm and 12 mm from the base metal. In comparison, block A shows a relatively uniform distribution of hardness and that is indicative of a homogenous microstructure at different heights in the building direction. In addition, the average width of the grains in blocks A and E was quantified from the transverse sections using the linear intercept method [39]. The results are shown in Table 3 and corroborate well with the trend observed in the hardness measurements, implying that the decrease in the hardness with an increase in the heat input is a consequence of an increase in the average grain width. This is due to the decrease in the cooling rate when the heat input increases, as the cooling rate varies

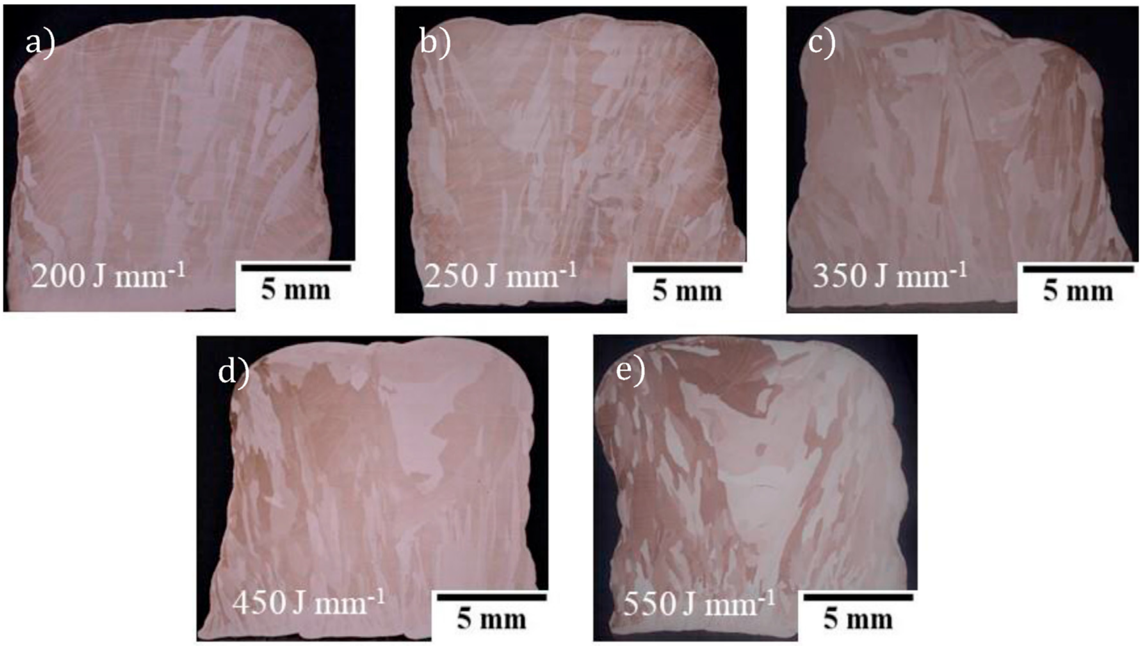

Fig. 5 – Optical micrographs of the transvers sections of the blocks showing the presence of columnar grains and grain coarsening in the top half section of block E. The micrographs were prepared at 45 mm from the starts of the deposits.

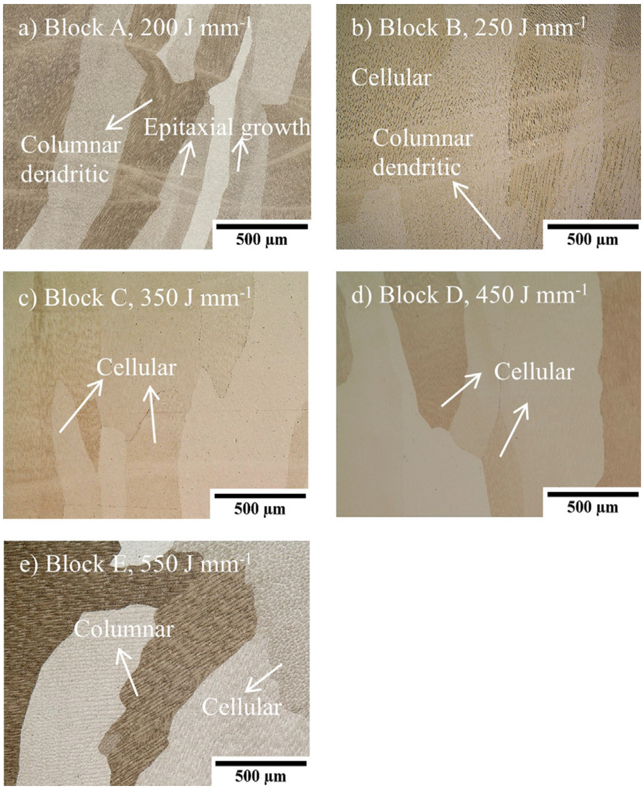

Fig. 6 – Optical micrographs of the transverse sections of the blocks showing the microstructural features.

Table 3 – Average grain width in blocks A and E as determined from the transverse sections.

Grain width in µm	Distance from base plate	
	5 mm	12 mm
Block A	270 ± 30	310 ± 20
Block E	390 ± 40	1120 ± 200

inversely with the heat input [40]. The reduction in the cooling rate subjects the single phase Invar 36 alloy to elevated temperatures for longer durations, consequently facilitating grain growth [41]. Therefore, increasing the heat input from 200 towards 550 J mm^{-1} was found to induce grain coarsening during the deposition of Invar 36, thereby reducing the hardness of the as-deposited alloy. The results of the XRF measurments performed on the five blocks are shown in Fig. 8. The Ni content in all the blocks was found to be maintained around 36 wt %, meaning that the increasing heat input did not lead to element loss due to burn-off. This is a critical aspect in Invar alloys since the lowest thermal expansion is observed at 36 wt % of Ni. All other elements are also within the range of the nominal chemical composition specified by the wire manufacturer. Furthermore, EDS was also utilised to analyse the chemical composition for any possible segregation of the alloying elements. However, the results were inconclusive and showed no clear trends. The absence of segregation could be a direct result of the thermal cycling during deposition. Invar 36 tends to have a low thermal diffusivity meaning that thermal energy is likely to accumulate with time [42]. Additionally, according to the equilibrium binary Fe–Ni phase diagram Invar 36 remains in the austenitic phase field in a broad temperature range (700 K–1700 K approx.) [43]. Therefore, as the deposition proceeds the availability of thermal energy will promote the balancing of compositional gradients that may have occurred during solidification given that sufficient time is available. The low thermal diffusivity along with the single phase nature of the Invar alloy also facilitates the coarsening of the grains with an increase in the heat input as described earlier. It should be noted that XRF and EDS was used in this study and these techniques provide a reasonable first impression of the chemical composition. However, the analysis of the composition, for example, at the level of micro-segregation can be considered for future work.

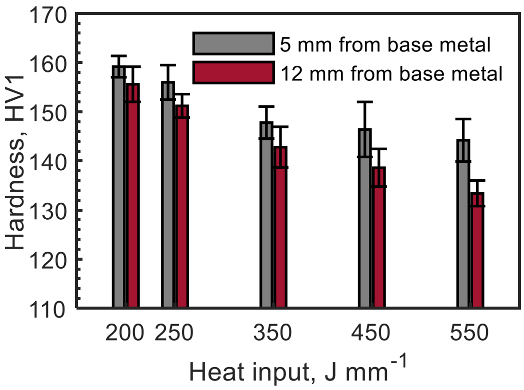

Fig. 7 – The results of the microhardness measurements performed on the transverse sections of the blocks.

The blocks deposited at the extreme condition of the heat inputs were analysed using XRD and the results are shown in Fig. 9. The blocks are found to be entirely austenitic, which is expected in Invar 36 as the binary Fe–Ni alloy system exists in the fcc structure above a Ni content of 30 at. % [44]. However, the indices of the maximum intensity peaks differ for block A and E in the figure. In block A, the peak with the maximum intensity is a result of reflections form the (100) planes whereas, in block E it is due to the reflections form (111) planes. To explain this, we refer to Fig. 5 that shows the macroscopic overview of all the blocks. The microstructure of block E is not homogeneous throughout the build as severe grain coarsening is observed in the top region of block E. The high heat input used for the deposition of block E led to this grain coarsening as the microstructure of block A is relatively homogenous after being deposited at a much lower heat input. Consequently, the large grains in block E may have dominated the Bragg criteria leading to the maximum reflection intensity from the (111) planes. Whereas the maximum intensity from (200) planes in the case of block A is expected since for cubic metals the preferential grain growth direction is <100> [45,46].

3.2. *Characterisation of cracking*

The blocks deposited at the heat inputs ranging from 250 to 550 J mm^{-1} were found to be susceptible to intergranular

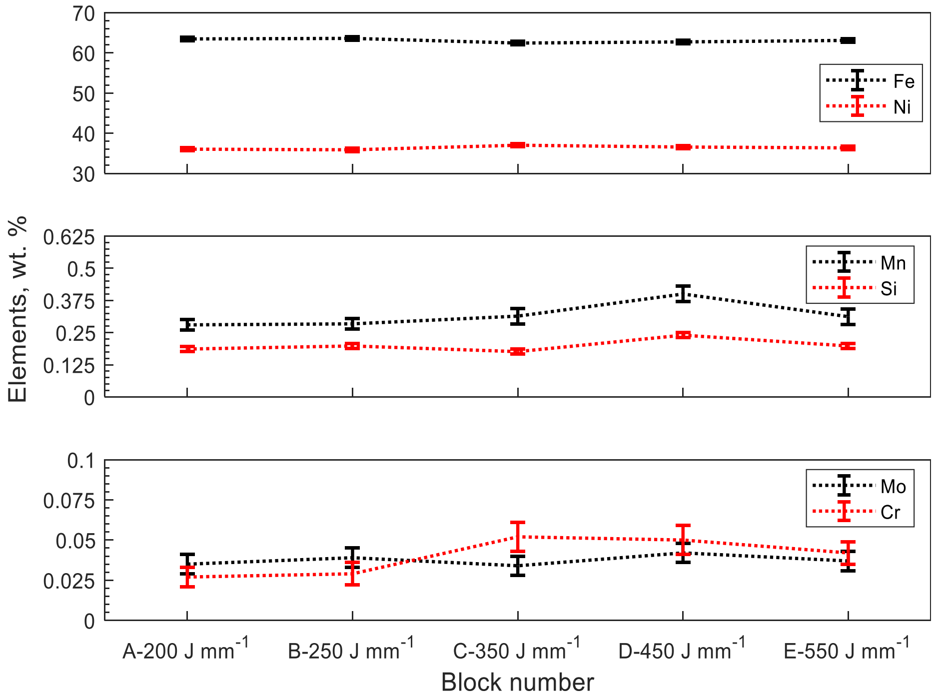

Fig. 8 – Major alloying elements in the as-deposited blocks as quantified from XRF measurements.

cracking. The effect of the heat input on the intensity of cracking is quantified in Fig. 10. The total crack length per block is used as a qualitative indicator for the susceptibility to cracking, and is found to increase with an increase in the heat input. The cracking observed in this study can be distinguished into micro and macro-cracking, depending on the heat input, as shown in Figs. 11 and 12, respectively. Cracking transforms from micro to macro-cracking above a heat input of 350 J mm^{-1} (block C). In the case of block B, the grain boundaries were generally found to be decorated with voids, along with small micro-cracks as shown in Fig. 11. This could represent the initial stage of crack initiation by void formation and coalescence. The micro-cracks in block B could only be concluded as cracks by SEM observation. Larger cracks were observed in block C and were wide enough for easy identification with optical microscopy. The length of the largest crack observed in blocks B and C were 0.6 mm and 0.8 mm, respectively. In comparison, the largest crack in blocks D and E measured 1.4 and 2.9 mm, respectively.

A further increase in the heat input resulted in large macro-cracks that were commonly observed in blocks D and E as shown in Fig. 12 (a) and (b), respectively. Some cracks were wide enough to allow for SEM observation of the crack flanks as shown in Fig. 13 for block E. At lower magnifications, the crack flanks appear flat and have a wavy morphology. The presence of rounded micro-voids (<1 μm in diameter) is revealed at a higher magnification and implies that there was limited ductility in the material during fracture. In other words, a quasi-cleavage fracture mechanism prevailed at the grain boundaries during WAAM of the Invar alloy in the heat inputs ranging from 250 to 550 J mm^{-1}, thereby resulting in

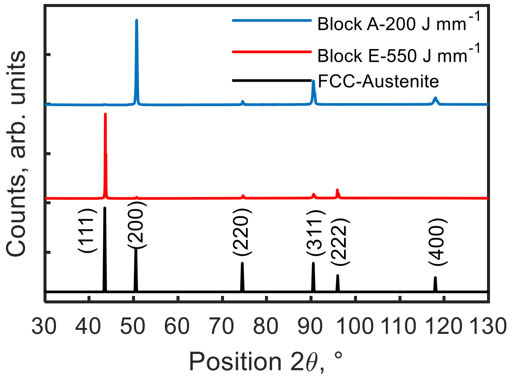

Fig. 9 – The XRD patterns of the as-deposited Invar alloy, blocks A and E.

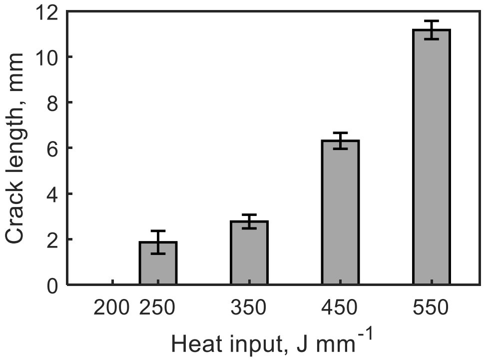

Fig. 10 – Experimentally derived variation of the crack length with the heat input. The average crack length per block is determined from observing four transverse sections taken at 35 mm, 40 mm, 45 mm and 50 mm from the starts of the deposits.

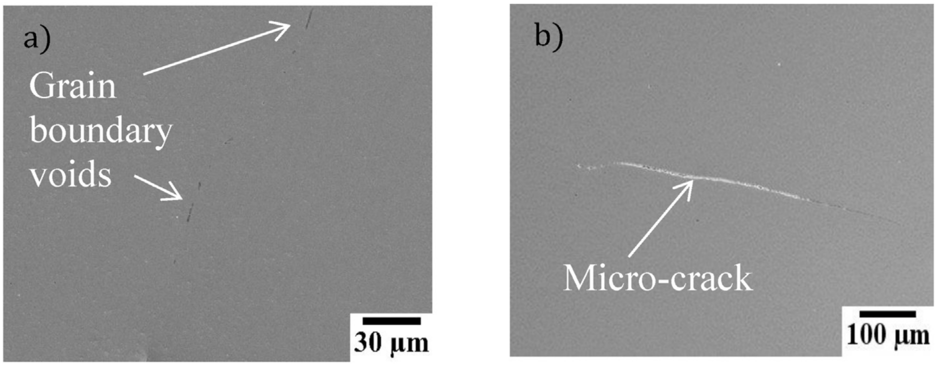

Fig. 11 – : SEM micrographs of a transverse section in block B (250 J mm^{-1}) showing voids at a grain boundary in (a) and a micro-crack in (b).

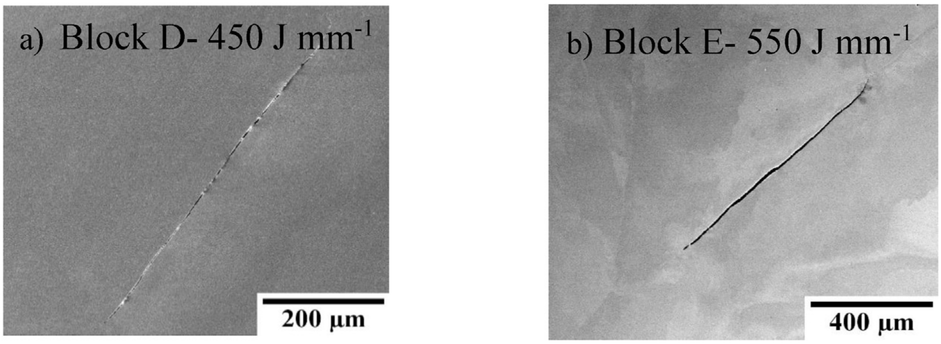

Fig. 12 – (A) and (b), SEM micrographs showing cracks in the transverse sections taken from blocks D and E, respectively.

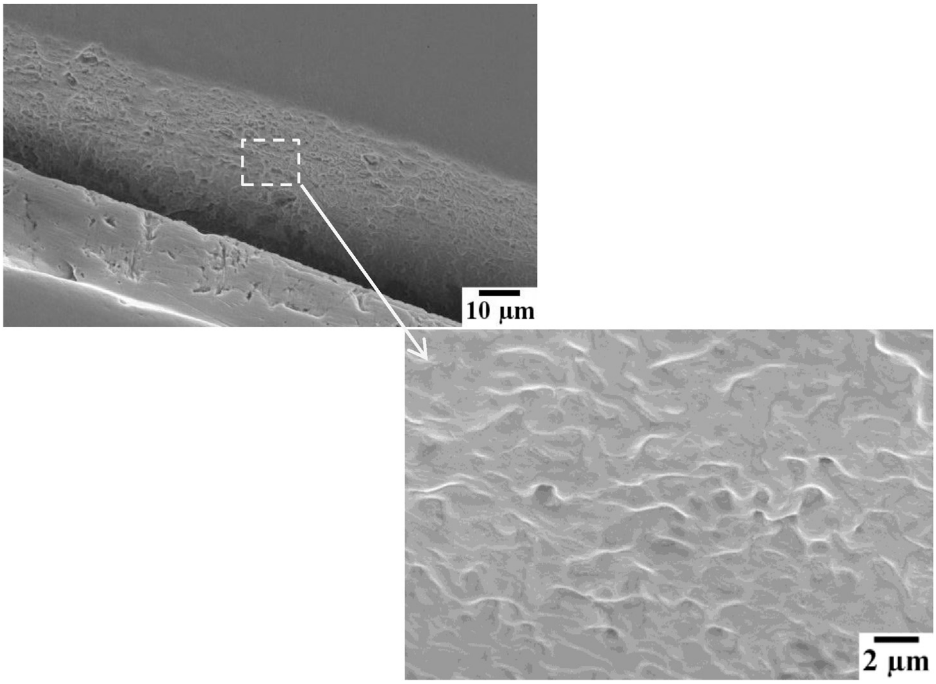

Fig. 13 – SEM micrographs of the crack flank at low and high magnification taken from block E (550 J mm^{-1}).

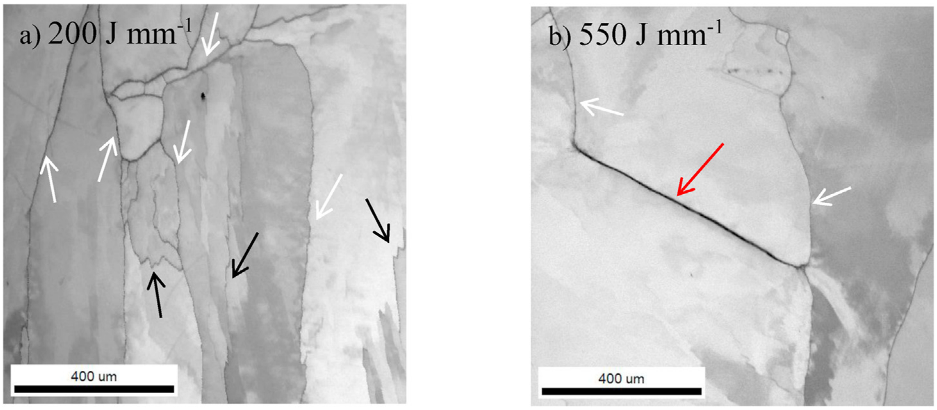

Fig. 14 – **(A) and (b) shows the image quality maps of transverse sections in blocks A and E, respectively.**

intergranular cracking. The absence of dendritic features on the fracture surface means that the cracking occurred in solid state. Additionally, enrichment of impurity elements like S and P was not detected during the chemical analysis of the crack flanks. Therefore, the occurrence of solidification cracking can be ruled out.

For further analysis, EBSD was utilised and the image quality (IQ) maps of samples taken from blocks A and E are shown in Fig. 14 (a) and (b), respectively. The highly non-tortuous character of the high angle grain boundaries with a misorientation more than 15° (white arrows) is noticeable in these maps. In Fig. 14 (a), serrated boundaries are also observed and are identified as low angle boundaries (black arrows) with a misorientation between 5° and 15°. The crack is identified to form along a high angle grain boundary (red arrow) in the IQ map corresponding to block E, whereas the IQ map of the sample from block A is free of cracks.

Due to the thermal cycles in AM non-uniform stresses/strains can be imposed on the deposited material. A qualitative assessment of these strains can be done through EBSD by plotting kernel average misorientation (KAM) maps. The KAM values, stated in degrees, represents residual strain as local variations in lattice orientation in the form of geometrically necessary dislocations (GNDs) [47,48]. In Fig. 15, the KAM maps are shown corresponding to the IQ maps of Fig. 14. High values of KAM are associated with areas around the crack and the triple point (red circle in Fig. 15 (b)) of the grains. This implies that strain was localised at these locations rather than being distributed throughout the matrix. The average KAM value calculated from both the maps is similar, 0.59° and 0.54° in Fig. 15 (a) and (b), respectively. The total length of the high and low angle grain boundaries calculated from Fig. 15 (a) is 5.7 mm and 2.4 mm, respectively, whereas in Fig. 15 (b) the lengths are 3.2 mm and 0.9 mm, respectively. The presence of a larger number of grain boundaries in the EBSD sample taken from block A, in comparison to the sample of block E, is also evident in the IQ maps shown in Fig. 14 (a) and (b). The higher grain boundary area in the KAM map of block A effectively promotes the partitioning of strain among several grain boundaries. As a result the triple point and the associated grain boundaries in

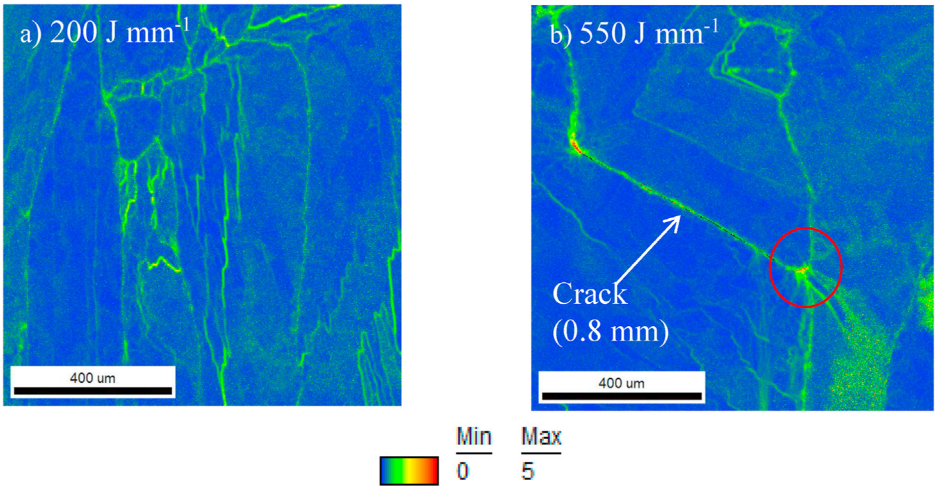

Fig. 15 – **(A) and (b) shows the kernel average misorientation maps corresponding to samples taken from blocks A and E, respectively.**

Fig. 15 (b), have to accommodate higher strains in comparison to Fig. 15 (a). A crack then forms if the built up strain at the grain boundary exceeds the strength of that grain boundary. In summary, the KAM maps give evidence of residual strain in the as-deposited Invar alloy. Despite the similar average KAM value in the two maps, cracking only occurs in the case of block E. This can be attributed to the higher heat input used for the deposition of block E that results in coarsening of the grains. Consequently, the strain that must be accommodated per grain boundary increases. Therefore, the susceptibility of the as-deposited Invar alloy to cracking increases as the heat input is increased from 200 towards 550 J mm^{-1} during the cold wire pulsed GTAW process. The increase in the heat input facilitates the coarsening of grains, that in turn increases the localisation of strain at the grain boundaries and leads to the nucleation of intergranular cracks.

The results of this section link the cracking observed during WAAM of Invar to ductility dip cracking (DDC). This is a solid-state cracking phenomenon that occurs when the transient build-up of stresses/strains can exhaust the limited ductility of a material at elevated temperatures [49]. A material specific temperature range is identified in which the ductility drops and is referred to as the ductility dip range. Ductility dip cracks are commonly reported in materials that display non-tortuous grain boundaries and are often associated with triple junctions of the grains [50]. Grain boundary sliding is one of the known mechanisms that leads to DDC [49–51]. In the studies pertaining to assess the weldability of Invar and Ni-base alloys, DDC cracks have been reported to have a similar morphology to the results shown in this section [52,53]. The role of grain boundary sliding in causing DDC was reported in a hot cracking study of Invar 36 [54]. Additionally, it has been shown in a weldability assessment study of Invar 36 that lowering the heat input improves the ductility dip range of the alloy [55]. This improvement means that a higher level of stress/strain can be tolerated before cracking occurs. Furthermore, a lowering of the heat input during wire-arc based DED of Invar can facilitate the reduction of strain localisation at a grain boundary, thereby improving the resistance to cracking as shown earlier in this section. Regarding the chemical composition, the effect of impurity elements like S and P is known to be deleterious with regards to DDC [8,56]. The Invar wire used in this study had extremely low levels of S and P as stated in Table 1. Additionally, enrichment of these elements at the grain boundaries/crack flanks during WAAM of Invar was not observed when analysed with EDS. Therefore, Invar alloy with relatively low amounts of S and P can still be susceptible to DDC owing to the transient built of stresses/strains during WAAM.

3.3. *Tensile testing of as-deposited invar*

The tensile properties of as-deposited Invar 36 in the case of the low heat input, crack free, condition of block A1 (200 J mm^{-1}) are shown in Fig. 16. These results are found to be in good agreement with the material properties specified by the Invar wire manufacturer. The average yield strength is found to be slightly lower, 6.6% and 5.2% for the samples oriented in Z and X directions, respectively, than the material specification of 280 MPa. Whereas, the average ultimate tensile strength and elongation from the tested samples surpassed the material specification of 350 MPa and 25%, respectively. No significant anisotropy was observed between the average tensile properties of the vertically and horizontally oriented samples. This agrees with the results of Veiga et al., as they report no directional anisotropy in the tensile properties of Invar 36 processed using gas metal arc welding [26]. However, they observed pronounced directional anisotropy in the tensile properties of Invar 36 processed using plasma arc welding. Macroscopically, the tensile samples were deformed with a cup and cone appearance following fracture, indicative of a ductile failure. One sample per direction is shown in Fig. 17, for the purpose of fractography. The fracture surface of the samples as observed in a SEM showed the presence of dimples. These observations are evidence of a ductile failure that is induced by void nucleation, growth, and coalescence. Whereas, in the case of Invar fabricated in the high heat input (550 J mm^{-1}) condition, the average tensile properties were found to be well below the specifications from the material supplier as listed in Table 4. This was due to the observation of premature failure in 6 out of 8 samples during testing. In two of the prematurely failed samples, failure was observed before the onset of yielding. This led to a complete brittle failure as seen in Fig. 18 (a). Some samples showed the presence of secondary cracks (white arrows) on the surface, apart from the main apart from the main fracture site as shown in Fig. 18 (b). It is likely that these cracks are a result of opening of the internal ductility dip cracks during tensile loading. The fracture surface of two samples (one per direction) as observed in a SEM is shown in Fig. 19. The macroscopic appearance of the samples and the presence of cleavage regions that are visible in the low magnification figures of the fracture surface suggest that the failure was predominantly brittle. The arrows in the figures indicate internal cracks and linearly arranged voids on the fracture surface. The internal cracks and voids could potentially be the fracture initiation sites as the sample has failed in the vicinity of these defects. In addition, such defects can act as stress concentrators, thereby increasing the likelihood of failure. These defects can be associated to the phenomenon of

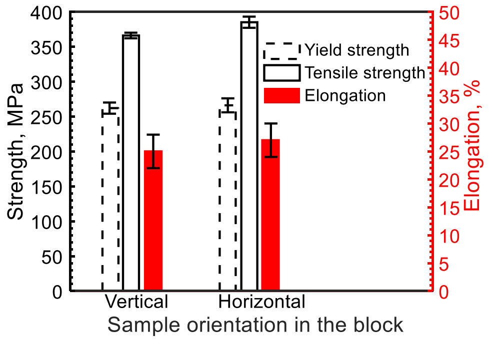

Fig. 16 – Tensile properties of the as-deposited Invar alloy in the low heat input condition of block A1, 200 J mm^{-1}. Vertical and horizontal samples oriented in Z and X directions, respectively. Material specifications: Yield Strength: 280 MPa, Ultimate Tensile Strength: 350 MPa and Elongation: 25%.

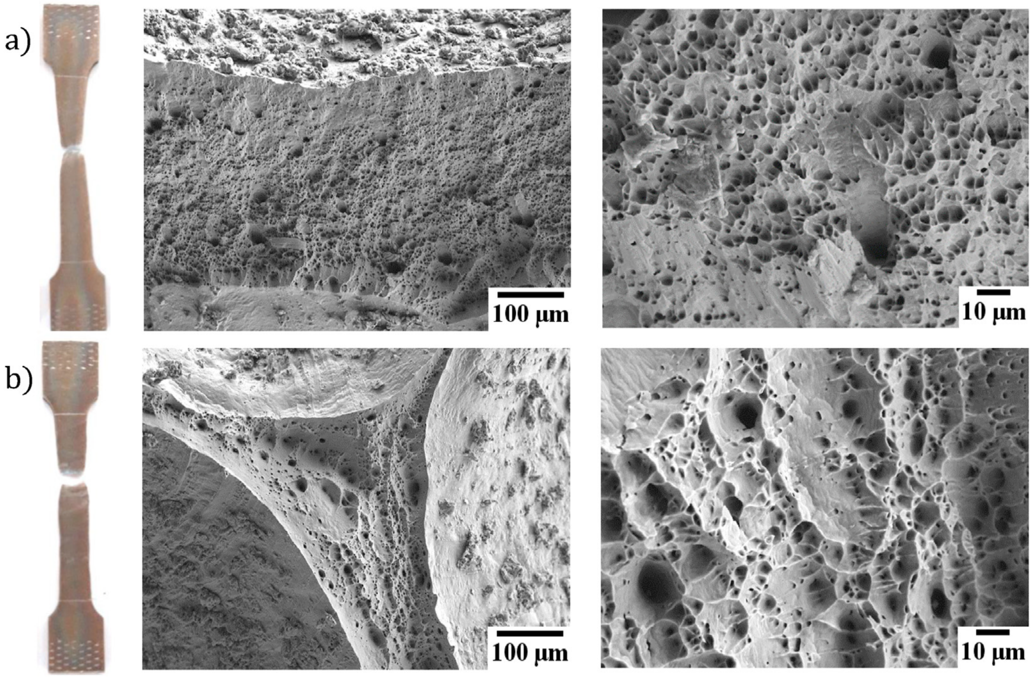

Fig. 17 – (A) and (b), shows the SEM micrographs of the fracture surface of the tensile samples taken from block A1 (200 J mm^{-1}) oriented in the building (Z) and travel direction (X), respectively.

ductility dip cracking that occurred during the deposition of Invar in the high heat input condition. Consequently, due to the presence of ductility dip cracks an inherently ductile alloy at room temperature (Invar 36) can become prone to brittle failure in a tensile loading environment. Since the same alloy when deposited in the low heat input (200 J mm^{-1}, crack free) condition displays a good mechanical response that agrees with the material specifications from the wire supplier.

3.4. *CTE of as-deposited invar*

The temperature-displacement curves of the as-deposited Invar 36 samples in the extreme conditions of the heat input are shown in Fig. 20. The curves for the four samples are nearly identical as seen from the insert in the figure. The variation of the thermal expansion with temperature is approximately linear in the temperatures between room temperature (RT) to 400 K, and 550 K onwards. Whereas, between 413 K and 540 K the variation is non-linear. In this temperature range, the mangnetrostrictive effect of Invar diminishes and the thermal expansion due to lattice vibrations takes over. Thereby, resulting in a normal thermal expansion behaviour at temperatures above 573 K as seen in the displacement curves shown in Fig. 20. However, Invar 36 still exhibits a much lower thermal expansion at temperatures above 573 K in comparison to stainless steel. The Curie temperature obtained from the displacement curves was found to be in the range of 550–555 K for the four samples and is in accordance with the value reported in the literature for Invar 36 [4].

The mean CTE of the as-deposited Invar alloy in the extreme conditions of the heat input are listed in Tables 5 and 6. The observed CTE values are on par with those reported for the conventionally processed Invar 36 [4,5]. Therefore, cold wire pulsed GTAW is a potential alternative to conventional and powder based processing of Invar 36. The as-deposited alloy in both conditions of the heat input exhibits the lowest CTE in the temperature range between RT and 373 K. In general, the CTE of the vertically built samples are slightly higher than the horizontally oriented sample in both conditions of the heat input as shown in Tables 5 and 6 The microstructure of the deposits showed columnar grains oriented along the building direction as shown earlier.

The disparity between the CTE of the vertical and horizontal samples cannot be attributed to the differences in the grain morphology/texture. This is due to the dependence of thermal expansion on the symmetry of the crystal, or in other words, the thermal expansion for a cubic system is isotropic regardless of the crystallographic direction [57]. Additionally, the low thermal expansion behaviour of Invar is highly dependent on the chemical composition. The XRF analysis on the blocks showed that the Ni content in all the blocks is maintained around 36 wt %, and the low thermal expansion Invar effect is most prominent at this content of Ni. The presence of other

Table 4 – Tensile properties of the as-deposited Invar alloy in the high heat input condition of block E1, 550 J mm^{-1}. Material specifications: Yield Strength (YS): 280 MPa, Ultimate Tensile Strength (UTS): 350 MPa and Elongation: 25%.

As-deposited Invar 550 J mm^{-1}	YS MPa	UTS MPa	Elongation %
Vertical (Z-direction)	237 ± 31	329 ± 41	26 ± 5
Horizontal (X-direction)	210 ± 69	269 ± 11	12 ± 9

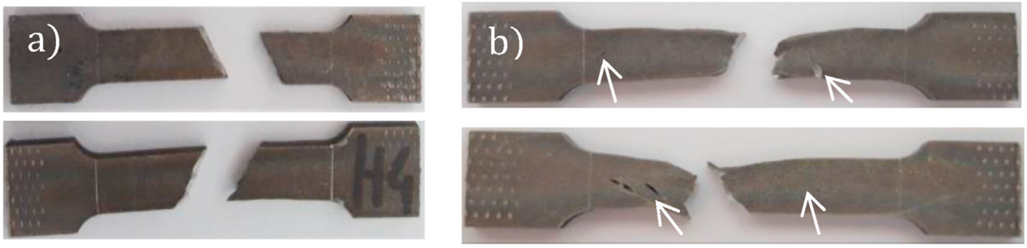

Fig. 18 – Tensile samples from block E1 (550 J mm^{-1}), showing a brittle failure in (a), cracks on the sample surface in (b).

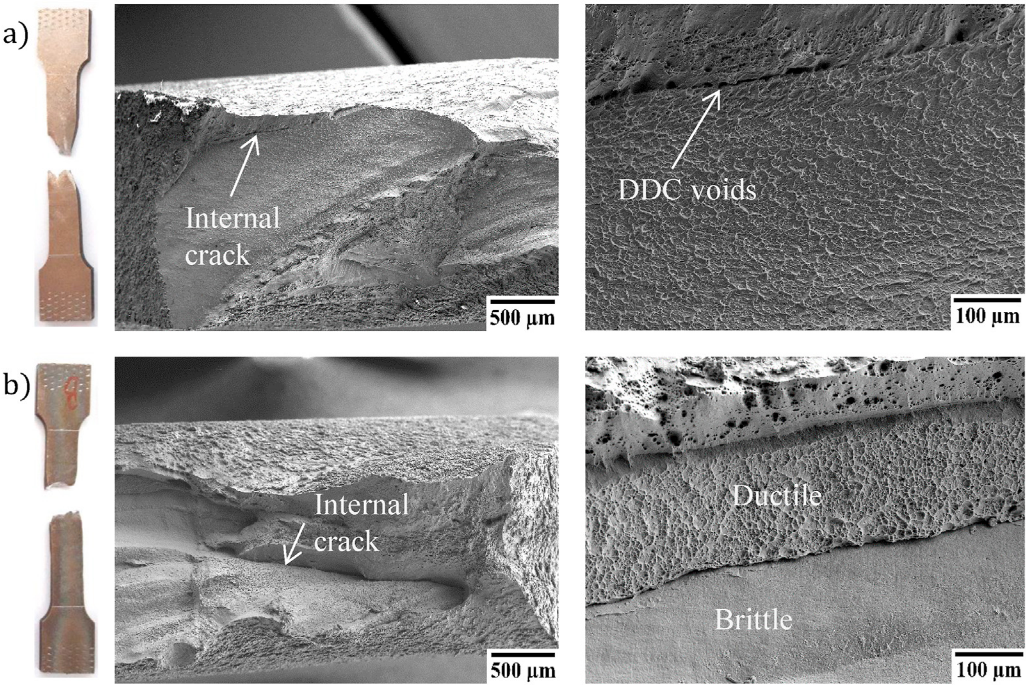

Fig. 19 – (A) and (b), shows the SEM micrographs of the fracture surface of the tensile samples taken from block E1 (550 J mm^{-1}) oriented in the building (Z) and travel direction (X), respectively.

alloying elements can influence the thermal expansion of Invar alloys however, any macroscopic enrichment/depletion of the other alloying elements is not observed between the blocks A and E. Consequently, the chemical composition cannot account for differences in the CTE values reported in Tables 5 and 6 However, under the influence of stress, thermal expansion can display anisotropic behaviour along different crystal directions [58]. It is well known that additively manufactured components can experience complex stress states [59]. The presence of residual stresses in Invar produced by selective laser melting was shown by Yakout et al. [60]. The stress states of the deposited parts were not quantified in this study

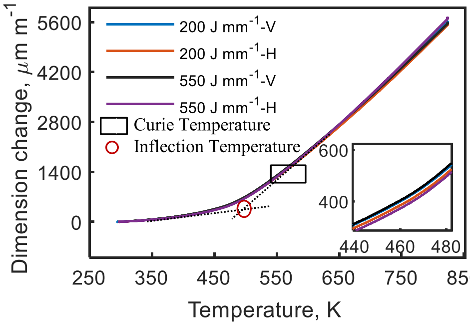

Fig. 20 – The displacement curves obtained from the dilatometry analysis of the as-deposited Invar alloy samples in the two extreme conditions of the heat input (200 and 550 J mm^{-1}). V (vertical) and H (horizontal) refer to samples oriented in the building (Z) and travel (X) directions, respectively.

Table 5 – The mean CTE of the as-deposited Invar alloy in the low heat input condition. The CTE values are in the unit of: $\times 10^{-6}$ K^{-1}, and the uncertainty in measurement: ±0.01 $\times 10^{-6}$ K^{-1}.

Mean CTE	200 J mm^{-1}, Vertical	200 J mm^{-1}, Horizontal
RT-373	1.40	1.39
RT-473	2.74	2.67
RT-573	5.85	5.73
RT-673	8.34	8.15

Table 6 – The mean CTE of the as-deposited Invar alloy in the high heat input condition. The CTE values are in the unit of: $\times 10^{-6}$ K^{-1}, and the uncertainty in measurement: $\pm 0.01 \times 10^{-6}$ K^{-1}.

Mean CTE	550 J mm^{-1}, Vertical	550 J mm^{-1}, Horizontal
RT-373	1.48	1.27
RT-473	2.79	2.60
RT-573	5.92	5.81
RT-673	8.32	8.36

however, it is safe to assume that the blocks will be subject to residual stresses. Therefore, the difference in the CTE between the vertically and horizontally built samples could arise from the residual stress sates experienced by the deposited blocks.

Lastly, the heat input used for depositing block E/E1 had led to intergranular cracking as pointed out earlier. Whereas cracking was avoided during the deposition of block A/A1 owing to the much lower heat input. The comparison of the CTE values between Tables 5 and 6 indicates that the presence of cracks barely affects the thermal performance of Invar. If the influence of the cracks were to be significant on the CTE, a clear disparity would be identified in the CTE values obtained from the samples extracted from blocks A1 and E1 as shown in Tables 5 and 6, respectively. Specifically in the low temperature regime (below the Curie temperature) where the lattice thermal expansion is countered by the spontaneous volume magnetostriction. On the other hand, the density of cracks and the width or size of the cracks could be important factors to consider while evaluating the effect of cracks on the thermal expansion of Invar. As it is possible that the effect of the cracks on thermal expansion becomes pronounced above a certain density of cracks. Similarly, the width/the size of the cracks, or quantified by the aspect ratio of the cracks, may also influence the thermal expansion. These factors were not explicitly considered in this study and are recommended for future work. However, the dilatometry samples taken from block E1 were machined in the vicinity of locations where intergranular cracks were observed through metallographic observations. Therefore, purely form the viewpoint of using Invar for its thermal expansion properties, the use of the high HI condition of block E1 may be justified. This indeed leads to the occurrence of intergranular cracking, but facilitates a higher deposition rate. As, in total 44 and 28 layers were needed to achieve similar heights in blocks A1 and E1, respectively. However, in situations where it is important to avoid cracks, specifically in tensile loading applications, it is necessary to lower the HI. Naturally, a crack free deposit with good expansion properties can then be obtained but at the cost of the deposition rate which in turn could be offset by using a multi-machine deposition approach.

4. Conclusions

This work was focussed on investigating the processability of Invar using a wire-based DED technique. The effect of the heat input on the microstructure, tensile behaviour, and thermal expansion of the Invar alloy was explored. Based on the experiments performed in this study it can be concluded that.

1. Cold wire GTAW can be employed for the fabrication of low thermal expansion Invar 36 without the presence of lack of fusion defects. In this aspect, using a suitable range for the wetting angle of the weld beads is critical during overlapping to avoid defects.
2. The microstructure of the as-deposited Invar alloy is mainly composed of columnar grains with non-tortuous grain boundaries. Additionally, due to the single phase nature of Invar 36, the alloy is prone to grain coarsening that can lead to the formation of ductility dip cracks.
3. The macroscopic Ni content in the as-deposited Invar alloy is maintained at 36 wt % and the alloy remains entirely austenitic at various processing conditions.
4. The susceptibility of Invar 36 to ductility dip cracking decreases with a reduction in the heat input. This is facilitated by the availability of an increased grain boundary area with a drop in the heat input, thereby distributing the built up strain among the grain boundaries.
5. Avoiding cracking is necessary in the structural applications of Invar 36 since the presence of intergranular cracks can lead to premature failure. Whereas, the mechanical properties of as-deposited Invar alloy in the crack free condition meet the specifications of the material supplier.
6. The mean CTE values of the as-deposited Invar 36 in the low (crack free) and the high (with intergranular cracks) heat input conditions are comparable to those displayed by the conventionally processed alloy.

CRediT authorship contribution statement

Arjun Sood: Conceptualisation, Methodology, Validation, Investigation, Resources, Writing- Original Draft, Visualisation. Jim Schimmel: Methodology, Validation, Investigation, Resources. Vitoria M. Ferreira: Resources. Marko Bosman: Resources, Funding Acquisition. Constantinos Goulas: Resources, Writing- Review & Editing, Supervision. Vera Popovich: Resources, Writing- Review & Editing, Supervision. M.J.M. Hermans: Resources, Writing- Review & Editing, Supervision, Project administration.

Declaration of competing interest

The authors declare that they have no known competing financial interests or personal relationships that could have appeared to influence the work reported in this paper.

Acknowledgements

This work was supported by the European Union's Horizon 2020 research and innovation programme under grant agreement no. 723699. This research is also supported by the Materials innovation institute M2i (www.m2i.nl). This publication reflects only the author's view and the Commission is not responsible for any use that may be made of the information it contains. Ruud Hendrikx and Richard Huizenga at the Department of Materials Science and

Engineering of the Delft University of Technology are acknowledged for the X-ray analysis. Dr. Martin Luckabauer at the faculty of Engineering and Technology of the University of Twente is acknowledged for facilitating the dilatometry analysis.

REFERENCES

[1] Nakamura Y. The invar problem. IEEE Trans Magn 1976:278–91.

[2] Shiga M. Lnvar alloys. Curr Opin Solid State Mater Sci 1996:340–8.

[3] Rancourt D, Dang M-Z. Relation between anomalous magnetovolume behavior and magnetic frustration in Invar alloys. Phys Rev B 1996:12225.

[4] Davis JR. In: Low-expansion alloys in *metals handbook desk edition*. ASM International; 1998.

[5] ASM Handbook Committee. Properties and selection: nonferrous alloys and special-purpose materials in *ASM handbook*, 2. ASM international; 1990.

[6] Thyssenkrupp. Stainless Steel 2017;316L:11 [Online]. Available: https://d2zo35mdb530wx.cloudfront.net/_legacy/UCPthyssenkruppBAMXUK/assets.files/material-data-sheets/stainless-steel/stainless-steel-1.4404-316l.pdf.

[7] S. Yamamo. World's first invar alloy LNG piping under the seabed. The 14th International Conference & Exhibition on Liquefied Natural Gas. Poster Session. PO-13.

[8] Ogawa T. Weldability of Invar and its large-diameter pipe. Weld J 1986:213–26.

[9] Corbacho J, Suárez J, Molleda F. Welding of invar Fe-36Ni alloy for tooling of composite materials. Weld Int 1998:966–71.

[10] Yakout M, Cadamuro A, Elbestawi M, Veldhuis SC. The selection of process parameters in additive manufacturing for aerospace alloys. Int J Adv Des Manuf Technol 2017:2081–98.

[11] Yakout M, Elbestawi M, Veldhuis SC. A study of thermal expansion coefficients and microstructure during selective laser melting of Invar 36 and stainless steel 316L. Additive Manufacturing; 2018. p. 405–18.

[12] Allen J. An investigation into the comparative costs of additive manufacture vs. machine from solid for aero engine parts. ROLLS-ROYCE PLC DERBY (UNITED KINGDOM); 2006 [conference paper].

[13] Williams SW, Martina F, Addison AC, Ding J, Pardal G, Colegrove P. Wire + arc additive manufacturing. Mater Sci Technol 2016:641–7.

[14] Huang SH, Liu P, Mokasdar A, Hou L. Additive manufacturing and its societal impact: a literature review. Int J Adv Des Manuf Technol 2013:1191–203.

[15] Herzog D, Seyda V, Wycisk E, Emmelmann C. Additive manufacturing of metals. Acta Mater 2016:371–92.

[16] Frazier WE. Metal additive manufacturing: a review. J Mater Eng Perform 2014:1917–28.

[17] Rodrigues TA, Duarte V, Miranda R, Santos TG, Oliveira J. Current status and perspectives on wire and arc additive manufacturing (WAAM). Materials 2019:1121.

[18] Ding D, Pan Z, Cuiuri D, Li H. Wire-feed additive manufacturing of metal components: technologies, developments and future interests. Int J Adv Des Manuf Technol 2015:465–81.

[19] Qiu C, Adkins NJ, Attallah MM. Selective laser melting of Invar 36: microstructure and properties. Acta Mater 2016:382–95.

[20] Harrison NJ, Todd I, Mumtaz K. Thermal expansion coefficients in invar processed by selective. J Mater Sci 2017:10517–25.

[21] Asgari H, Salarian M, Ma H, Olubamiji A, Vlasea M. On thermal expansion behavior of invar alloy fabricated by modulated laser powder bed fusion. Mater Des 2018:895–905.

[22] Khanna N, Mistry S, Rashid RR, Gupta MK. Investigations on density and surface roughness characteristics during selective laser sintering of Invar-36 alloy. Mater Res Express 2019:086541.

[23] Yang Q, Wei K, Yang X, Xie H, Qu Z, Fang D. Microstructures and unique low thermal expansion of Invar 36 alloy fabricated by selective laser melting. Mater Char 2020:110409.

[24] Strauss J, Stucky M. Laser additive manufacturing processing of a mixture of iron and nickel powders. In: Proceedings of the 27th Solid Freeform Fabrication Symposium; 2016 Aug 10. p. 8–10. Austin, USA.

[25] Tan H, Wang Y, Wang G, Zhang F, Fan W, Feng Z, et al. Investigation on microstructure and properties of laser solid formed low expansion Invar 36 alloy. J Mater Res Technol 2020:5827–39.

[26] Veiga F, Suárez A, Artaza T, Aldalur E. Effect of the heat input on wire-arc additive manufacturing of invar 36 alloy: microstructure and mechanical properties. Weld World 2022:1081–91.

[27] Aldalur E, Suárez A, Veiga F. Thermal expansion behaviour of Invar 36 alloy parts fabricated by wire-arc additive manufacturing. J Mater Res Technol 2022;19:3634–45.

[28] Fowler J, Nycz A, Noakes M, Masuo C, Vaughan D. Wire-arc additive manufacturing: invar deposition characterization. In: International solid freeform fabrication symposium; 2019. Austin. 2019.

[29] Li F, Guo W, Lin B, Qi B, Chen L, Yu W, et al. Interfacial microstructure and mechanical properties of Fe-36Ni invar alloy GTAW joint. Indian J Eng Mater Sci 2017:290–4.

[30] Corbacho JL, Suárez JC, Molleda F. Grain coarsening and boundary migration during welding of invar Fe-36Ni alloy. Mater Char 1998:27–34.

[31] Nakagawa H, Matsuda F, Nagai A, Sakabata N. Weldability of Fe-36% Ni alloy (report I): hot cracking with cross-bead test (materials, metallurgy, weldability). In: Transactions of JWRI; 1980. p. 197–204.

[32] Norrish J. Recent gas metal arc welding (GMAW) process developments: the implications related to international fabrication standards. Weld World 2017;61(4):755–67.

[33] Kou S. Welding metallurgy. third ed. John Wiley & Sons; 2021. p. 37–60 [Chapter 2], Heat Flow in Welding.

[34] Mittal Arcelor [Online]. Available: www.spacematdb. [Accessed 28 September 2022]. https://www.spacematdb.com/spacemat/manudatasheets/Invar%20M93.pdf.

[35] The International Organization for Standardization. ISO 6507-1:2018(en) Metallic materials — vickers hardness test — Part 1: test method [Online]. Available: https://www.iso.org/obp/ui/#iso:std:iso:6507:-1:ed-4:v1:en. [Accessed 4 November 2022].

[36] The International Organization for Standardization. ISO 6892-1:2019(en) Metallic materials — Tensile testing — Part 1: Method of test at room temperature 2019;11 [Online]. Available: https://www.iso.org/obp/ui/#iso:std:iso:6892:-1:ed-3:v1:en. [Accessed 4 November 2022].

[37] ASTM International Committee E37 on Thermal Measurements. Standard test method for linear thermal expansion of solid materials by thermomechanical analysis. ASTM International; 2014.

[38] Kou S. Welding metallurgy. third ed. John Wiley & Sons; 2021. p. 209–46 [Chapter 9],Nucleation and Growth of Grains.

[39] ASTM International. Standard test methods for determining average grain size [Online]. Available: https://www.astm.org/e0112-13r21.html; 2021. November 2022.

[40] Jafari D, Vaneker TH, Gibson I. Wire and arc additive manufacturing: opportunities and challenges to control the

quality and accuracy of manufactured parts. Mater Des 2021;202:109471.

[41] Rosli NA, Alkahari MR, bin Abdollah MF, Maidin S, Ramli FR, Herawan SG. Review on effect of heat input for wire arc additive manufacturing process. J Mater Res Technol 2021;11:2127–45.

[42] Yakout M, Elbestawi M, Veldhuis S, Nangle-Smith S. Influence of thermal properties on residual stresses in SLM of aerospace alloys. Rapid Prototyp J 2019;26:213–22.

[43] Vernyhora I, Tatarenko V, Bokoch S. Thermodynamics of fcc-Ni–Fe alloys in a static applied magnetic field, 2012. ISRN Thermodynamics; 2012.

[44] McKeehan L. The crystal structure of iron-nickel alloys. Phys Rev 1923;21:402.

[45] Kurz W, Fisher DJ. Fundamentals of solidification. 1984.

[46] Tiller WA. Preferred growth direction of metals. J Occup Med 1957;9:847–55.

[47] Min X, Emura S, Chen X, Zhou X, Tsuzaki K, Tsuchiya K. Deformation microstructural evolution and strain hardening of differently oriented grains in twinning-induced plasticity beta titanium alloy. Mater Sci Eng, A 2016;659:1–11.

[48] Zhang X, Chen H, Xu L, Xu J, Ren X, Chen X. Cracking mechanism and susceptibility of laser melting deposited Inconel 738 superalloy. Mater Des 2019;183:108105.

[49] Lippold JC. Welding metallurgy and weldability. John Wiley & Sons 2014:130–207 [Chapter 4], Solid State Cracking.

[50] Kou S. Welding metallurgy. third ed. John Wiley & Sons; 2020. p. 379–97 [Chapter 14], Ductility Dip Cracking.

[51] Lippold JC, Kiser SD, DuPont JN. Welding metallurgy and weldability of nickel-base alloys. John Wiley & Sons; 2011. p. 47–156 [Chapter 3], Solid-Solution Strengthened Ni-base alloys.

[52] Zhang Y-C, Nakagawa H, Matsuda F. Weldability of Fe-36% Ni alloy (report VI): further investigation on mechanism of reheat hot cracking in weld metal (materials, metallurgy & weldability). Trans JWRI 1985;14(2):325–34.

[53] Collins M, Ramirez A, Lippold J. An investigation of ductility dip cracking in nickel-based weld metals-Part II: fracture behavior and fracture surface morphology are related to microstructure, composition, and temperature. Weld J 2003;82(12):348–54.

[54] Zhang Y-C, Nakagawa H, Matsuda F. Weldadility of Fe-36% Ni alloy (report V): behaviors of grain-boundary sliding and cavity formation preceding reheat hot cracking in weld metal (materials, metallurgy & weldability). Trans JWRI 1985;14(2):319–24.

[55] Zhang Y-C, Nakagawa H, Matsuda F. Weldability of Fe-36% Ni alloy (report III): dynamic observation of reheat hot crack and evaluation of hot ductility of reheated weld metal (materials, metallurgy & weldability). Trans JWRI 1985;14(1):107–14.

[56] Matsuda F, Nakagawa H, Minehisa S, Sakabata N, Ejima A, Nohara K. Weldability of Fe-36% Ni alloy (report II) : effect of chemical composition on reheated hot cracking in weld metal(materials, metallurgy & weldability). Trans JWRI 1984;13(2):241–7.

[57] Cullity BD, Graham CD. Introduction to magnetic materials. John Wiley & Sons; 2011.

[58] Honda K, Foundation HM. Physics and applications of invar alloys. Maruzen; 1978.

[59] Carpenter K, Tabei A. On residual stress development, prevention, and compensation in metal additive manufacturing. Materials 2020;13(2):255.

[60] Yakout M, Elbestawi M, Veldhuis S, Nangle-Smith S. Influence of thermal properties on residual stresses in SLM of aerospace alloys. Rapid Prototyp J 2020;26(1):213–22.